Zhang *et al. PhotoniX* (2024) 5:17
https://doi.org/10.1186/s43074-024-00132-9

PhotoniX

RESEARCH Open Access

Cascaded chiral birefringent media enabled planar lens with programable chromatic aberration

Dewei Zhang[1], Chun-Ting Xu[1*], Quan-Ming Chen[1], Han Cao[1], Hong-Guan Yu[1], Qing-Gui Tan[2], Yan-qing Lu[1*] and Wei Hu[1*]

*Correspondence: xuchunting@nju.edu.cn; yqlu@nju.edu.cn; huwei@nju.edu.cn

[1] National Laboratory of Solid State Microstructures, Key Laboratory of Intelligent Optical Sensing and Manipulation, College of Engineering and Applied Sciences, Nanjing University, Nanjing 210023, China
[2] National Key Laboratory of Science and Technology on Space Microwave, China Academy of Space Technology, Xi'an, China

Abstract

Wavefront control is the fundamental requirement in optical informatics. Planar optics have drawn intensive attention due to the merits of compactness and light weight. However, it remains a challenge to freely manipulate the dispersion, hindering practical applications, especially in imaging. Here, we propose the concept of frequency-synthesized phase engineering to solve this problem. A phasefront-frequency matrix is properly designed to encode different spatial phases to separate frequencies, thus makes arbitrary dispersion tailoring and even frequency-separated functionalization possible. The periodically rotated director endows cholesteric liquid crystal with a spin and frequency selective reflection. Moreover, via presetting the local initial orientation of liquid crystal, geometric phase is encoded to the reflected light. We verify the proposed strategy by cascading the chiral anisotropic optical media of specifically designed helical pitches and initial director orientations. By this means, planar lenses with RGB achromatic, enhanced chromatic aberration and color routing properties are demonstrated. Inch-sized and high-efficient lenses are fabricated with low crosstalk among colors. It releases the freedom of dispersion control of planar optics, and even enables frequency decoupled phase modulations. This work brings new insights to functional planar optics and may upgrade the performance of existing optical apparatuses.

Keywords: Liquid crystals, Planar lens, Dispersion programmable, Spatial light modulation

Introduction

Light, thanks to its intrinsic multiple dimensions and massive parallelism, has been used as an information carrier in vital fields such as optical communications, optical computing, and information displays. Wavefront modulation is crucial for all above applications [1, 2]. Traditional refractive and reflective optics work based on propagation phase accumulation, thus suffering from bulky size and heavy weight. Recently, light modulation techniques have been developed toward compactness, integration, and multifunction. Planar optics based on artificial subwavelength resonators [3, 4] or patterned birefringent materials [5, 6] have been broadly investigated due to the merits of flatness and

© The Author(s) 2024. **Open Access** This article is licensed under a Creative Commons Attribution 4.0 International License, which permits use, sharing, adaptation, distribution and reproduction in any medium or format, as long as you give appropriate credit to the original author(s) and the source, provide a link to the Creative Commons licence, and indicate if changes were made. The images or other third party material in this article are included in the article's Creative Commons licence, unless indicated otherwise in a credit line to the material. If material is not included in the article's Creative Commons licence and your intended use is not permitted by statutory regulation or exceeds the permitted use, you will need to obtain permission directly from the copyright holder. To view a copy of this licence, visit http://creativecommons.org/licenses/by/4.0/.

compactness. One typical element is the planar lens, through which light diffracts and interferes to perform functions such as focusing, collimating, imaging and beam splitting [7–9]. Similar to other diffractive elements, the generated phase profiles of such lenses exhibit strong wavelength dependency. The deviation here is caused by structural dispersion and determined only by structure parameters. This drastically hinders practical usage in both industry and scientific research. Achromatic lenses are highly pursued in photography, astronomy and microscopy to eliminate dispersion blurs [10]. On the contrary, for applications such as spectrometer, hyperspectral imaging and color routing, large chromatic aberration is favored for separating various colors more significantly [11, 12]. Therefore, it is an urgent pursuit to explore an effective way to program the chromatic aberration of planar optics.

Several strategies have been developed to solve this problem. Firstly, an extra wavelength-dependent modulation factor $\phi(\lambda)$ is introduced to realize broadband phase compensation of the planar optics [13]. For instance, compensation between dynamic phase and geometric phase is realized by specifically designing resonators of a metalens [14–16] or integrating a liquid crystal layer with a metalens [17]. The combination of a refractive lens of positive dispersion and a diffractive lens of negative dispersion forms an achromatic lens [18, 19]. Secondly, discrete wavelengths are encoded with separate phases to realize an equivalent achromatic aberration. Three primary colors are filtered, phase modulated separately and then remixed to eliminate the chromatic aberration [20–22]. A spatial multiplex method based on computational holography is adopted to realize the same function [21, 23]. However, this strategy suffers from discrete frequency and low efficiency. More recently, broadband achromatic lenses have been fabricated by optimizing the spectral degrees of freedom in the lens phase profiles [24] or introducing light frequency-domain coherence optimization [25]. Despite this impressive progress, a new approach toward the programable chromatic dispersion of planar lenses with large size, high efficiency and compact design is still urgently pursued. Liquid crystal (LC) is an excellent candidate for functional planar optics due to the pronounced self-assembly property of anisotropic media. Various geometric-phase devices have been presented based on patterned liquid crystals [26] or stacking specially designed RGB off-axis lenses [27]. However, these devices also exhibit strong wavelength-dependent dispersion. Cholesteric LC (CLC) [28–31], featuring a periodic helical structure, exhibits spin-selective Bragg reflection. Light within the band is selectively reflected and encoded with a geometric phase determined by the initial orientation of the CLC, while light outside the band transmits and can carry a uniform phase delay [32, 33]. The color-filtered phase encoding makes CLC perfectly suitable for individual phasefront engineering at separate frequencies.

In this work, we establish a general frequency synthesized phase engineering framework to encode different spatial phases to separate frequencies. By properly designing the phasefront frequency matrix, arbitrary dispersion tailoring and frequency-separated functionalization can be realized. The helical birefringent medium CLC is adopted to demonstrate the above design because of the frequency-selective geometric phase encoding. Through stacking multiple CLC layers with specifically designed helical pitch and lens profiles, inch-sized planar lenses with RGB achromatic, enhanced chromatic aberration and color routing properties are presented. The focusing efficiency reaches

85.3% for selective spin. The proposed approach breaks the diffractive dispersion limitation of planar optics and may significantly improve their performance.

Results

Frequency-synthesized phase engineering

The angular spectrum dispersion of the diffractive lens leads to variations in focal length and image distance among different colors, causing color distortions or blurs in an image. To solve this problem, we propose a frequency-synthesized phase engineering framework. The point of the idea is to encode different phasefronts to separate colors and thus program the chromatic dispersion or even realize distinguished functions for a series of colors. It can be depicted as

$$\begin{bmatrix} E(x,y)^{out}_{\lambda_1} \\ E(x,y)^{out}_{\lambda_2} \\ \vdots \\ E(x,y)^{out}_{\lambda_n} \end{bmatrix} = \begin{bmatrix} e^{i\varphi(x,y)\lambda_1} & & & \\ & e^{i\varphi(x,y)\lambda_1} & & \\ & & \ddots & \\ & & & e^{i\varphi(x,y)\lambda_n} \end{bmatrix} \times \begin{bmatrix} E(x,y)^{in}_{\lambda_1} \\ E(x,y)^{in}_{\lambda_2} \\ \vdots \\ E(x,y)^{in}_{\lambda_n} \end{bmatrix} \tag{1}$$

where$E(x,\ y)^{out}$ means the output field, $E(x,\ y)^{in}$ means the input field, the term$\left[e^{i\varphi(x,\ y)}\right]$ is the phasefront-frequency matrix and subscripts$\{\lambda_1,\ \lambda_2\ \cdots,\ \lambda_n\}$ indicate different wavelengths. With diagonal elements $e^{i\varphi(x,\ y)}$, different spatial phases are encoded to separate wavelengths (Fig. S1). For a given $E(x,\ y)^{in}$, through properly designing $e^{i\phi(x,\ y)}$, one can achieve a uniform $E(x,\ y)^{out}$ for different λ. That is the principle to design an achromatic lens. Moreover, $E(x,\ y)^{out}$ can be freely modulated for individual λ, thus enabling arbitrary functionalization for separate frequencies. It supplies a practical framework for planar lenses with programable chromatic dispersion.

RGB achromatic lens based on an optimized phasefront-frequency matrix

The left scheme in Fig. 1a depicts the negative chromatic aberration of conventional diffractive lenses. Here, a RGB achromatic design for a planar lens is proposed by optimizing the phasefront-frequency matrix (right image in Fig. 1a). To focus a white light onto a single spot, the entire wave should propagate according to a wavelength-dependent hyperbolic phase profile [34],

$$\varphi_{r,\lambda} = -\frac{2\pi}{\lambda}\left(\sqrt{r^2+f^2}-f\right) \tag{2}$$

where λ, r and f are the wavelength, radial coordinate and focal length, respectively. The radial distance of the first phase change of 2π with respect to the center is defined as the feature size R. When $r = R$, *i.e.*, $\phi_{(R,\lambda)} = 2\pi$, Eq. (2) can be rewritten as [35],

$$f_{(R,\lambda)} = \frac{R^2}{2\lambda} - \frac{\lambda}{2} \tag{3}$$

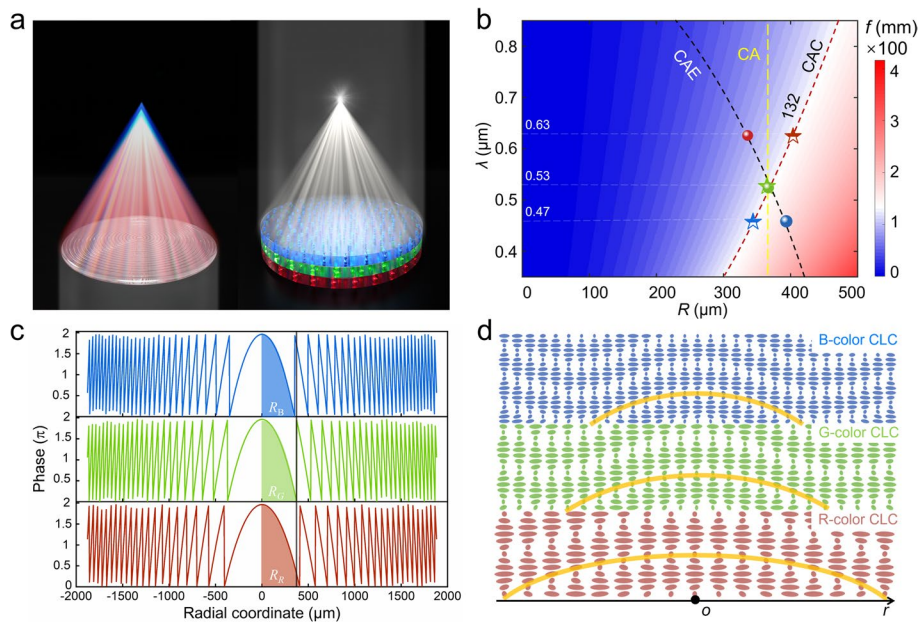

Fig. 1 Phasefront-frequency matrix optimization for a RGB achromatic lens. **a** (left) Chromatic aberration of a traditional diffractive lens and (right) RGB achromatic of phasefront-frequency matrix-optimized planar lens. **b** Dependency of focal length *f* on feature size *R* and wavelength λ. The red dashed line reveals a chromatic aberration-corrected (CAC) line for $f = 132$ mm, the yellow dashed line shows the normal chromatic aberration of a diffractive lens with $R = 375$ μm, and the black dashed line indicates a chromatic aberration-enhanced (CAE) case. The color bar indicates *f* varying from 0 mm to 400 mm. **c** Design of RGB achromatic lenses by encoding corrected $\varphi_{(R,\lambda)}$ to RGB colors separately. **d** Schematic sectional image of a three-layer cascaded CLC lens with precisely designed helical pitches *p* and optimized phase profiles $(\varphi_B, \varphi_G, \varphi_R)$. The orange arches indicate equiphasic surfaces. Names are labelled at top right of each layer

Figure 1b is drawn according to Eq. (3) and vividly reveals the dependency of f on λ and R. The yellow dashed line exhibits the negative chromatic aberration (CA) of a conventional diffractive lens with $R = 375$ μm. The red dashed line marks a chromatic aberration-corrected (CAC) line for $f = 132$ mm. The design can be realized by properly correcting R for different λ to satisfy Eq. (3). The previously proposed frequency synthesized phase engineering can perfectly solve this problem. To be brief, three primary colors are chosen as examples. We fix $f(\lambda_R) = f(\lambda_G) = f(\lambda_B) = 132$ mm ($\lambda_R = 630$ nm, $\lambda_G = 530$ nm, $\lambda_B = 470$ nm) and then encode corrected $f_{(R,\lambda)}$ to R, G, and B separately (Fig. 1c). CLC provides an ideal platform for frequency synthesized phase engineering. Only light within the reflection band is selectively encoded with a geometric phase $\left(|R\rangle e^{-i\cdot 2\alpha}\right)$ [30, 36]. Therefore, the CAC design can be realized by stacking three CLC layers with specific helical pitches and patterned initial helix orientations (Fig. 1d, Fig. S2b, c). Theoretically, frequency-synthesized phase engineering is suitable for arbitrarily tailoring the chromatic aberration of planar lenses (Fig. S2a). For instance, a chromatic-aberration-enhanced (CAE) lens, as marked by the black dashed line in Fig. 1b, can be achieved by introducing R opposite to λ changes.

Cascaded CLC RGB achromatic lens

Photoalignment polarization holography (PAPH) is adopted to imprint objective geometric phases with different R into the initial orientation of the CLC helix. Figure 2a vividly presents the principle of PAPH. The target linear polarization distribution is obtained by the interference between a right-circularly polarized (RCP) plane wave (reference) and left-circularly polarized (LCP) light with a template lens phase, which are represented by the North and South Poles on the Poincaré sphere, respectively [37]. The generated electric field (right image in Fig. 2a) is calculated as

$$\begin{bmatrix} 1 \\ i \end{bmatrix} e^{-i\vec{k_1}\vec{r}} + \begin{bmatrix} 1 \\ -i \end{bmatrix} = 2e^{i\frac{\varphi}{2}} \begin{bmatrix} \sin\frac{\varphi}{2} \\ \cos\frac{\varphi}{2} \end{bmatrix} \tag{4}$$

where $k_1 = 2\pi/\lambda_0(\text{-}\sin\theta, 0, \cos\theta)$ and $k_2 = 2\pi/\lambda_0(0, 0, 1)$ indicate the wavevectors of LCP and RCP light, respectively. $\lambda_0 = 405$ nm denotes the laser wavelength for PAPH.

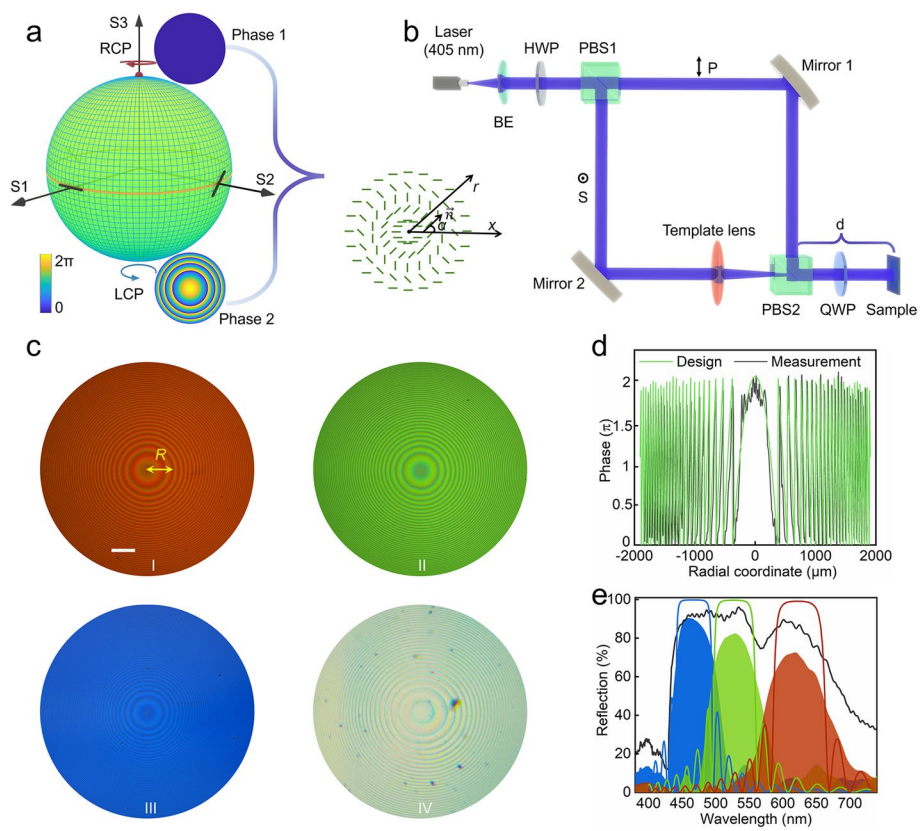

Fig. 2 Fabrication and characterization of a cascaded CLC RGB achromatic lens. **a** Principle scheme of polarization holography. Two phase diagrams of orthogonal circular polarizations are labeled at the South and North Poles on the Poincaré sphere. The color bar indicates the phase change from 0 to 2π. The right image reveals the interfered linear polarization distribution. **b** Optical setup for polarization holography. BE, HWP, QWP, and PBS indicate beam expanding, half-waveplate, quarter-waveplate, and polarization beam splitter, respectively. **c** POM micrographs of single channel (I, II, III) and cascaded RGB (IV, bottom to top) CLC lenses. The yellow bar indicates *R*, while the white scale bar indicates 300 μm. **d** Designed (green line) and measured (black line) hyperbolic phase profiles of the green-color selective CLC lens. **e** Simulated (solid lines) and experimental (solid regions) reflections of separated R, G, and B selective CLC lenses. The black line reveals the reflection of a cascaded CLC RGB achromatic lens

Linear polarization with a spatial distribution of $\phi/2 = \pi/\lambda_0 \sin\theta \cdot x$ is generated, where θ is the angle between k_1 and k_2 (Supplementary Note). A Mach-Zehnder interferometer is utilized to carry out the PAPH (Fig. 2b). The generated vector beam perpendicularly guides the local orientation of the photoalignment agent (azo dye, SD1) and further controls the initial orientation of the CLC helix. To maintain $f = 132$ mm, three different glass lenses with $f = 200$ mm, $f = 175$ mm and $f = 150$ mm are selected as template lenses according to $f = \lambda_0 d/\lambda$ for RGB colors, respectively. Notably, the optical path between the template lens and PBS2 equals that between the sample and PBS2 to perfectly match the equal-intensity condition (Fig. S3).

We adjusted the concentration of the chiral dopant to tune the central wavelength of the Bragg reflection. Polarization holograms record objective patterns to CLCs (10 mm in radius and 2 μm in thickness). The standing helix forms a Grandjean texture that exhibits a uniform brilliant color consistent with the photonic band gap (Fig. 2c, Fig. S4). The cross-section of the cascaded RGB CLC lens is shown in Fig. S6, with a total thickness of 6.4 μm. When the lens is observed in the reflection mode under a polarization optical microscope (POM), alternating bright and dark rings twice the number of designed 0–2π phase changes are revealed. The obtained phase profiles satisfactorily match the designs. Here, the hyperbolic phase profile of the green color-selective CLC lens $\lambda_G = 530$ nm is presented as an example (Fig. 2d), while additional details of the samples are provided in Fig. S5. The R of the RGB lens patterns is 403 μm, 376 μm, and 334 μm, respectively, which are in good agreement with the designs. The measured central wavelengths are 470 nm, 530 nm, and 630 nm, respectively, which are also consistent with the simulations. The reflection band of the cascaded CLC RGB achromatic lens is the superposition of individual RGB lenses. The reflection within the designed channel is one order larger than those of unselected channels (Supplementary Table 2). Therefore, modulating the phase of one color channel will not affect the phase modulation of the other channels. For long wavelengths (e.g. red light), the less pitches induce a lower Bragg reflection (Fig. 2e). Therefore, red light exhibits a lower reflectance with the cascaded CLC RGB achromatic lens. However, this issue can be satisfactorily addressed by increasing the layer thickness (Fig. S7).

Chromatic aberration-corrected imaging

Figure 3a exhibits the optical setup for characterizing the focusing and imaging performances of the cascaded CLC lens. The RGB and white light output from the supercontinuum laser are expanded and collimated to 12 mm then incident normally to the object mask (pluggable), whose image is reconstructed on the screen by the cascaded CLC lens. Firstly, f of RGB light is detected. The longitudinal intensity distributions in the x-z plane reveal a confocal length of 132 mm, which is in agreement with the FDTD simulations (Fig. 3b, Fig. S8a). Point spread function characterizations reveal that the full width at half-maximum (FWHM) of RGB light are 18 μm, 16 μm, and 15 μm, respectively. To verify the achromatic aberration of the proposed CLC CAC lens, we have compared it performance with a broadband CLC lens with the same optical setup (Fig. 3a). As shown in Fig. 3c, the letter "E" and the Chinese character "Light" are both clearly imaged in equal size on the same image plane for RGB incidences, respectively (Fig. 3c). Corresponding white light images are clearly observed as well. In contrast, images obtained

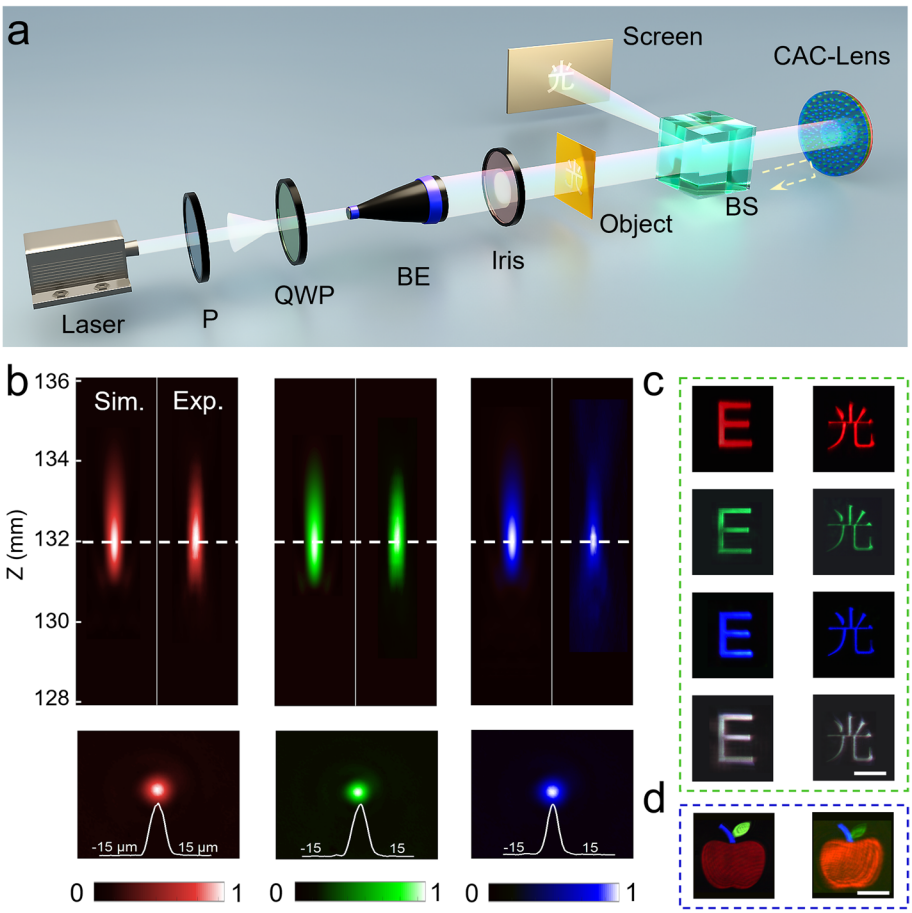

Fig. 3 Chromatic aberration-corrected imaging of the cascaded CLC lens. **a** Optical setup for the focusing and imaging characterization of the cascaded CLC lens. P, Polarizer; QWP, quarter-wave plate; BE, beam expander; BS, beam splitter. **b** Simulated (left) and experimental (right) results of longitudinal focusing cross sections in different colors. Focal plane intensity distributions and focal spot profiles (bottom) of RGB incidences, respectively. **c** RGB and white light imaging of a cascaded CLC lens (green frame). The scale bar indicates 500 μm. **d** RGB-color apple images formed by a commercial achromatic doublet (left, $f = 150$ mm) and fabricated CLC CAC lens (right). The scale bar indicates 2 mm

with conventional diffractive lenses suffer from intensive dispersion blurs (Fig. S8b). Figure 3d (right) show an RGB-color apple image formed by our cascaded CLC CAC lens. The slight image distortion compared to that formed by achromatic doublet (left) is attributed to the spherical aberration of the cascaded lens and the coma aberration from the central position mismatch among separate layers. It can be improved via introducing non-spherical phase profile and increasing the alignment accuracy (Fig. S8c). The difference in brightness is caused by the different attenuation ratio of light in our measurements to avoid overexposure on CCD (Fig. S9). The entire Group No. 3 of the USAF resolution target is clearly observed with the cascaded CLC lens, verifying the excellent imaging performance of the proposed lens design (Fig. S8d).

Chromatic aberration-enhanced zoom imaging

In contrast to the RGB achromatic imaging of a CAC lens, the CAE lens enhances the chromatic dispersion and thus enables zoom imaging by simply shifting the illuminating

wavelength [11]. As shown in Fig. 4a, masks of letters C, A, and E are placed at different positions, i.e., object lengths S_1, S_2, and S_3, respectively. The image distance is fixed at $2f_G$. When varying the incident wavelength, images of different letters are clearly captured by the CCD in different colors and amplifications. To verify the spectral zoom imaging, R of the CAE-lens is exchanged for R and B colors (Fig. 4b). Therefore, the R values of the RGB lens patterns in the CAE lens are 334 μm, 376 μm, and 403 μm (Fig. S10a, b). Due to the enhanced chromatic dispersion, RGB colored lights are focused at different focal lengths by the CAE lens. As presented in Fig. 4c, the obtained f_R = 94 mm, f_G = 132 mm, and f_B = 171 mm. Obviously, RGB colors are totally separated in the x-z plane because the depth of focus (λ/NA^2) is negligible compared to the variation in wavelength-dependent f. It suggests a zoom imaging with no crosstalk among colors (Fig. S10c). The focusing efficiency reaches 85.3% for 470 nm with an NA of 0.058. The size of the captured images changes significantly for RGB colors (Fig. 4d left). The maximum zoom factor reaches 3.2. According to the parameters of the CAE lens, wavelengths and sizes of captured images, the position and size of objects can be precisely reconstructed (Fig. 4d right, Fig. S10d, e). CAE lens zoom imaging is promising in non-mechanical optical tomography with the merits of rapid operation, high stability, and compact design.

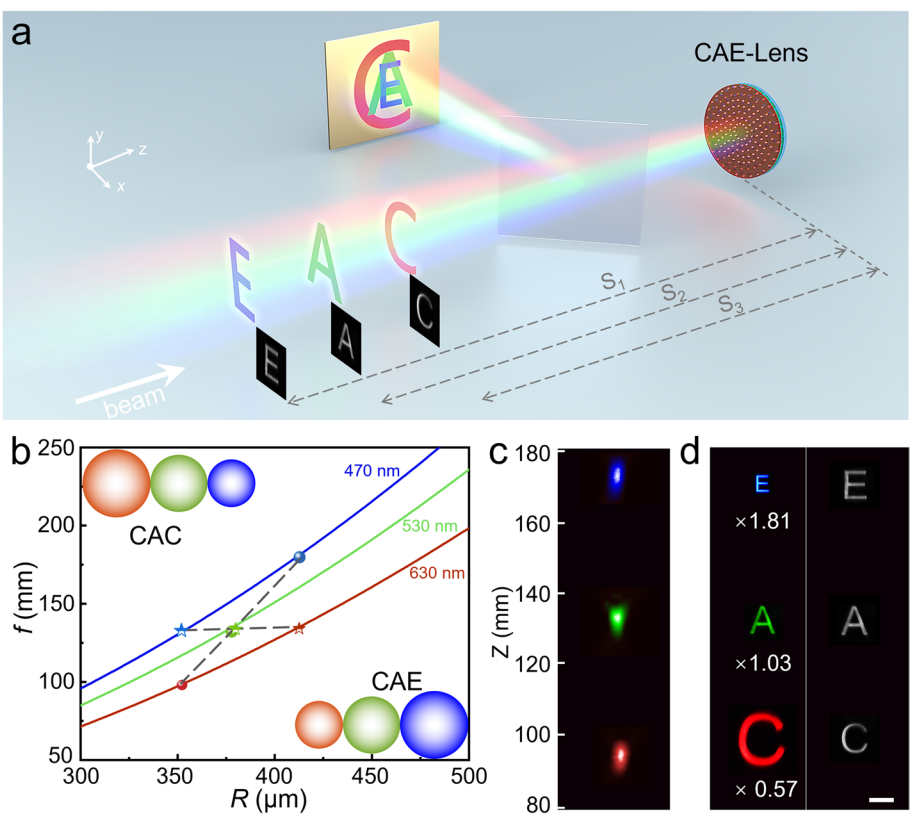

Fig. 4 Chromatic aberration-enhanced imaging of a cascaded CLC lens. **a** The optical setup for zoom imaging. Three pictures at different positions (S_1, S_2, S_3) are captured on the same imaging plane at different magnifications and different colors. **b** Dispersion engineering of the cascaded CLC lens based on the dependency of f on R. **c** Focal spots at x-z cross sections for RGB incidences, respectively. **d** Spectral zoom images (left) captured on the imaging plane of the CAE lens and the objects (right) reconstructed from the spectral zoom images. The scale bar indicates 500 μm

Cascaded off-axis CLC lens enabled color routing

Since E_{out} can be freely modulated for individual λ, functionalization for separate frequencies thus can be arbitrarily programmed. Here, we encode the phase diagram of a polarization grating and its conjugated phase diagram to the R and B channels, separately. The combined phase diagrams are expressed as

$$\varphi_{\text{total}} = \varphi_{\text{lens}} \pm \varphi_{\text{grating}} = -\frac{2\pi}{\lambda}\left(\sqrt{r^2+f^2}-f\right) \pm \frac{2\pi}{\lambda}\sin\beta \cdot x \tag{5}$$

Where β is the diffraction angle. Phase diagrams of ϕ_{lens} - ϕ_{grating}, ϕ_{lens}, $\phi_{\text{lens}} + \phi_{\text{grating}}$ and corresponding output wave vectors k_{out} are plotted for wavelengths of 630 nm, 530 nm, and 470 nm, respectively. The size of the lens is set to 20 mm × 20 mm (Fig. 5a). With such an off-axis CLC lens, beams of RGB colors are individually focused at designed positions [38] (Fig. 5a, top right inset). The off-axis lens combines a slanted polarization grating and a lens, and parabolic phase schemes for the R and B channels are presented in Fig. 5b. When observed under POM at 1000 times magnification, only the transverse linear phase change causing bright-dark alternations is revealed, which

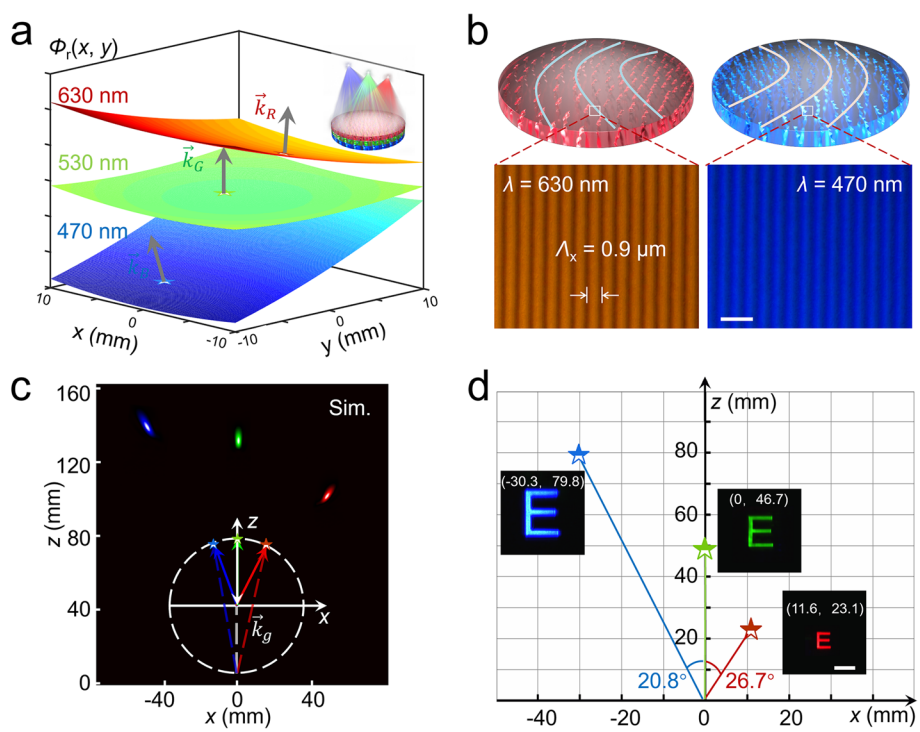

Fig. 5 Cascaded off-axis CLC lens for color routing. **a** Simulated *f* and *k* of a 20 mm × 20 mm CLC lens with Bragg-reflection central wavelengths of 630 nm, 530 nm and 470 nm. The top-right inset illustrates the function of the cascaded off-axis CLC lens. **b** Schematic illustration of CLC-lens (φ_{lens}- φ_{grating}, $\varphi_{\text{lens}} + \varphi_{\text{grating}}$) at $\lambda = 470$ nm and $\lambda = 630$ nm, respectively, and corresponding micrographs in the square marked regions recorded in the reflective mode under POM. The scale bar indicates 2 μm. **c** Simulated *x*-*z* section for RGB incidences. Schematic relationship among input, output and grating vectors for different wavelengths that satisfy the Bragg condition ($k_{\text{in}} + k_{\text{grating}} = k_{\text{out}}$). **d** Spatial multispectral imaging based on the cascaded off-axis CLC lens. The scale bar indicates 1 mm

alternates once within each period of the grating (~ 0.9 μm) (Fig. 5b). For normal incidence within the Bragg band, the beam is deflected with diffraction angle $\beta(x, y) = 2\gamma(x, y)$, where $\gamma = \arcsin(p/2\Lambda_x)$ is the inclination angle of the $k_{grating}$, which is related to the CLC pitch p and the lateral period of the polarization grating Λ_x (Fig. S11) [39]. Here, the CLC pitches are set 300 nm and 400 nm to obtain Bragg central wavelengths of 470 nm and 630 nm, respectively. Accordingly, $\beta_B = -19.2°$, $\beta_R = 25.6°$ when $\Lambda_x = 0.9$ μm. The focusing performances in the *x*-*z* plane of the off-axis CLC-lens are simulated (Fig. 5c). $\beta_B = -20.5°$, $\beta_G = 0°$ and $\beta_R = 24.2°$, which are consistent with the triangular relationship $k_{in} + k_{grating} = k_{out}$. Figure 5d shows the experimental spatial multispectral imaging of the off-axis CLC-lens. The object distance (*s*) is fixed at 184 mm, and RGB colored images of the letter "E" are projected to the predesigned directions in different magnifications.

Discussion

The above results suggest that the frequency-synthesized phase engineering framework endows planar lens outperforms already reported achromatic lenses in terms of aperture, efficiency, and multifunctionality, as presented in Supplementary Table 4. However, there is still room for improvement in transmission and transflective mode extending, dynamic operation, narrowband selectivity, polarization independency, and arbitrary functionalization. For example, 1), Transmissive frequency-synthesized phase engineering can be achieved by cascading different photopatterned multi-twist retarders [40]. Additionally, combining two materials can reasonably be expected to endow transreflective optics with frequency and spin divided functions [41]. 2), To achieve active modulation, separate CLC cells can be introduced to replace the LCP layers, whose pitches can be shifted both optically or electrically [31, 36]. For function reconfiguring, photo-rewriting can be adopted to reset the alignment of CLC inside such cells, separately [42]. 3), By reducing the birefringence of CLC, the bandwidth of Bragg reflection can be further narrowed, enabling dispersion tailoring in smaller frequency intervals. By changing the pitch, lattice constants and orienting the helix axis of CLC, modulations on wavelength, wave vector as well as geometric phase can be achieved [43, 44]. 4), Through introducing opposite handed CLCs, the orthogonal components of CP can be modulated simultaneously, making the cascaded CLC device more efficient and polarization independent [45]. 5), Besides PAPH, the spatial initial director orientations can also be manipulated by direct laser writing [46] or DMD based photo patterning [42], facilitating the arbitrary functionalization for separate frequencies.

Conclusions

A frequency-synthesized phase engineering framework is established to encode different spatial phases to individual frequencies. It endows planar optics with arbitrary dispersion tailoring and frequency-separated functionalization via designing the phasefront frequency matrix. The frequency-selective geometric phase encoding is demonstrated with the helical birefringent medium CLC. Through locally presetting the initial orientation of CLC, geometric phase is encoded to the Bragg reflected light, while the band can be precisely tailored by tuning the helical pitch. Via stacking multiple CLC layers, CAC, CAE as well as color-routing lenses with merits of large size (20 mm in diameter), high efficiency (85.3% for CP incidence), thin thickness (< 10 μm) and low crosstalk among

colors are presented (Supplementary Table 3). This work extends the knowledge on relationship between structures and functions, and brings new insights to functional planar optics. This approach releases the freedom of dispersion control of planar optics, and even enables frequency decoupled phase modulations. It will upgrade the performance of existing optical apparatuses that are widely utilized in optical imaging, computing, communicating and information displays.

Materials and methods

Materials

Photoalignment agent sulfonic azo dye SD1 (NCLCP, China) is dissolved in N, N-dimethylformamide at a weight concentration of 0.3%. The CLC mixture consists of reactive mesogen RM257 (NCLCP, China), chiral dopant R5011 (NCLCP, China), photoinitiator Omnirad651 (BASF, Germany) and surfactant EHA (Adamas-beta, China), and then is solved in toluene. The helical twisting power of R5011 in RM257 is 108 μm^{-1}. The concentration of R5011 in precursor is adjusted to control the helical pitch of the CLC. Detailed weight ratios are listed in Supplementary Table 1.

Lens fabrications

The SD1 solution is spin-coated onto a clean glass substrate at 800 rpm for 5 s, followed by 3000 rpm for 40 s and is annealed at 100 °C for 10 min to form the photoalignment film. Then, the sample is exposed using the set up as shown in Fig. 2b. Single-longitudinal-mode laser (DLC HOLO-LITHO 405, Toptica) is adopted as the light source and an exposure dose of 5 J/cm^2 is used. The CLC solution is spin-coated for 30 s at a speed of 2000 rpm and then heated at 80 °C for 2 min to evaporate residual solvent. Samples are cured under UV irradiation (365 nm) at a dose of 3 J/cm^2 in a nitrogen-rich environment. For cascaded CLC lenses, RGB CLC films are vertically stacked and each lens is spin-coated twice, which are separated by 100-nm silicon oxide layers.

Optical characterizations

Photographs are captured under the reflective mode of a polarization optical microscope (Nikon 50i POL, Japan). Reflection spectra are recorded with a spectrometer (ASC-UVNIR1, JCOPTIX, China). RGB-Color apple pattern is generated by a LCOS (Tianmu-I-020-L, Smartvision, China). Diffraction patterns are captured by a CCD (BGS-SP620, Ophir-Spiricon, USA) or a digital camera (EOSM, Canon, Japan). A super continuous fiber laser (SuperK EVO, NKT Photonics, Denmark) is utilized for focusing and imaging characterizations. A multichannel acousto-optic tunable filter (SuperK SELECT, NKT Photonics, Denmark) is adopted to generate monochromatic or mixed white lasers of 470 nm, 530 nm, and 630 nm. A polarizer and a quarter-wave plate (QWP) are employed to transfer LP to RCP. A collimator, a beam expander and an adjustable aperture are used to form a parallel beam in proper diameter. Bragg reflections of the CLC lenses are redirected by the beam splitter (BS) and finally captured by a CCD (Fig. 3a).

Numerical simulations

The finite-difference time-domain simulation package (Ansys Lumerical FDTD) is used to investigate the focusing of CLC lenses. Three-dimensional simulations are performed

under the boundary conditions of a perfectly matched layer, and the refractive indices n_o and n_e of the LC are set to be 1.51 and 1.69, respectively. The scattering coefficient for each LC layer is represented by $f(s)$, thus the reflectivity through n layers is $(1\text{-}f(s))^n$. However, as $f(s)$ is very small due to the ordered CLC, as well as the low refractive index mismatch at CLC/SiO_2 interfaces, we set $f(s) = 0$ in our simulation. PB phases of lenses are provided by the three-dimensional spatial distribution of LC (Fig. S7b). 470 nm, 530 nm, and 630 nm light in circularly polarization are used as light sources. Power intensity distributions at focus planes and *x*-*z* plane are evaluated using the same type of monitor.

Abbreviations

CLC Cholesteric liquid crystal
CAC Chromatic aberration-corrected
CAE Chromatic aberration-enhanced

Supplementary Information

The online version contains supplementary material available at https://doi.org/10.1186/s43074-024-00132-9.

Supplementary Material 1.

Acknowledgements
Not applicable.

Authors' contributions
W. Hu, Q. Tan and Y. Lu guided the project. D. Zhang, C. Xu, Q. Chen and W. Hu conceived the idea and designed the experiment. D. Zhang, H. Cao and H. Yu performed the experiments and measurements. W. Hu revised the manuscript. All authors analyzed the experimental data, drew the figures and prepared the manuscript. All authors read and approved the final manuscript.

Funding
This work was supported by the National Key Research and Development Program of China (2022YFA1203703), the National Natural Science Foundation of China (NSFC) (62035008), the Stable Support Fund of State Administration Science Technology and Industry for National Defense (HTKJ2022KL504003), and Fundamental Research Funds for the Central Universities (021314380233).

Availability of data and materials
The data that support the findings of this study are available from the corresponding author upon reasonable request.

Declarations

Ethics approval and consent to participate
Not applicable.

Consent for publication
All authors agree with the publication.

Competing interests
The authors declare no competing interests.

Received: 4 January 2024 Revised: 28 March 2024 Accepted: 22 April 2024
Published online: 06 May 2024

References

1. Malek SC, Overvig AC, Alu A, Yu N. Multifunctional resonant wavefront-shaping meta-optics based on multilayer and multi-perturbation nonlocal metasurfaces. Light Sci Appl. 2022;11:246.
2. Spagele C, et al. Multifunctional wide-angle optics and lasing based on supercell metasurfaces. Nat Commun. 2021;12:3787.
3. Yu N, et al. Light propagation with phase discontinuities: generalized laws of reflection and refraction. Science. 2011;334:333–7.
4. Sun S, et al. Gradient-index meta-surfaces as a bridge linking propagating waves and surface waves. Nat Mater. 2012;11:426–31.
5. Chen P, Wei BY, Hu W, Lu YQ. Liquid-crystal-mediated geometric phase: from transmissive to broadband reflective planar optics. Adv Mater. 2020;32:e1903665.

6. Chen QM, Xu CT, Liang X, Hu W. Helical structure endows liquid crystal planar optics with a customizable working band. Adv Quantum Technol. 2023;6:2200153.
7. Meem M, et al. Broadband lightweight flat lenses for long-wave infrared imaging. Proc Natl Acad Sci U S A. 2019;116:21375–8.
8. Hua X, et al. Ultra-compact snapshot spectral light-field imaging. Nat Commun. 2022;13:2732.
9. Khorasaninejad M, Capasso F. Metalenses: versatile multifunctional photonic components. Science. 2017;358:1146.
10. Chen WT, et al. A broadband achromatic metalens for focusing and imaging in the visible. Nat Nanotechnol. 2018;13:220–6.
11. Chen C, et al. Spectral tomographic imaging with aplanatic metalens. Light Sci Appl. 2019;8:99.
12. Arbabi E, Arbabi A, Kamali SM, Horie Y, Faraon A. Controlling the sign of chromatic dispersion in diffractive optics with dielectric metasurfaces. Optica. 2017;4:625–32.
13. Chen WT, Zhu AY, Capasso F. Flat optics with dispersion-engineered metasurfaces. Nat Rev Mater. 2020;5:604–20.
14. Wang S, et al. A broadband achromatic metalens in the visible. Nat Nanotechnol. 2018;13:227–32.
15. Aieta F, Kats MA, Genevet P, Capasso F. Multiwavelength achromatic metasurfaces by dispersive phase compensation. Science. 2015;347:1342–5.
16. Balli F, Sultan M, Lami SK, Hastings JT. A hybrid achromatic metalens. Nat Commun. 2020;11:3892.
17. Shen Z, et al. Liquid crystal integrated metalens with tunable chromatic aberration. Adv Photonics. 2020;2:036002.
18. Li Y, et al. Broadband cholesteric liquid crystal lens for chromatic aberration correction in catadioptric virtual reality optics. Opt Express. 2021;29:6011–20.
19. Zhan T, et al. Practical chromatic aberration correction in virtual reality displays enabled by cost-effective ultra-broadband liquid crystal polymer lenses. Adv Opt Mater. 2020;8:2000170.
20. Avayu O, Almeida E, Prior Y, Ellenbogen T. Composite functional metasurfaces for multispectral achromatic optics. Nat Commun. 2017;8: 14992.
21. Chen WT, et al. Dispersion-engineered metasurfaces reaching broadband 90% relative diffraction efficiency. Nat Commun. 2023;14:2544.
22. Zhou Y, et al. Multilayer noninteracting dielectric metasurfaces for multiwavelength metaoptics. Nano Lett. 2018;18:7529–37.
23. Li Z, et al. Meta-optics achieves poly-chromatic focusing for virtual reality. Sci Adv. 2021;7:eabe4458.
24. Shrestha S, Overvig AC, Lu M, Stein A, Yu N. Broadband achromatic dielectric metalenses. Light Sci Appl. 2018;7:85.
25. Xiao X, et al. Large-scale achromatic flat lens by light frequency-domain coherence optimization. Light Sci Appl. 2022;11:323.
26. Jiang M, et al. Low f-number diffraction-limited pancharatnam-berry microlenses enabled by plasmonic photopatterning of liquid crystal polymers. Adv Mater. 2019;31:e1808028.
27. Xiong J, Zhong H, Cheng D, Wu S-T, Wang Y. Full degree-of-freedom polarization hologram by freeform exposure and inkjet printing. PhotoniX. 2023;4:35.
28. Kobashi J, Yoshida H, Ozaki M. Planar optics with patterned chiral liquid crystals. Nat Photonics. 2016;10:389–92.
29. Rafayelyan M, Tkachenko G, Brasselet E. Reflective spin-orbit geometric phase from chiral anisotropic optical media. Phys Rev Lett. 2016;116: 253902.
30. Barboza R, Bortolozzo U, Clerc MG, Residori S. Berry phase of light under bragg reflection by chiral liquid-crystal media. Phys Rev Lett. 2016;117: 053903.
31. Xu CT, et al. Heliconical cholesterics endows spatial phase modulator with an electrically customizable working band. Adv Opt Mater. 2022;10:2201088.
32. Chen P, et al. Digitalizing self-assembled chiral superstructures for optical vortex processing. Adv Mater. 2018;30:1705865.
33. Kobashi J, Yoshida H, Ozaki M. Polychromatic optical vortex generation from patterned cholesteric liquid crystals. Phys Rev Lett. 2016;116: 253903.
34. Khorasaninejad M, et al. Metalenses at visible wavelengths: diffraction-limited focusing and subwavelength resolution imaging. Science. 2016;352:1190–4.
35. Zhao M, et al. Phase characterisation of metalenses. Light Sci Appl. 2021;10:52.
36. Chen P, et al. Chirality invertible superstructure mediated active planar optics. Nat Commun. 2019;10:2518.
37. Xiong J, Wu ST. Planar liquid crystal polarization optics for augmented reality and virtual reality: from fundamentals to applications. eLight. 2021;1:3.
38. Chen BH, et al. GaN metalens for pixel-level full-color routing at visible light. Nano Lett. 2017;17:6345–52.
39. Yin K, He Z, Wu ST. Reflective polarization volume lens with small f-number and large diffraction angle. Adv Opt Mater. 2020;8:2000170.
40. Li L, Shi S, Escuti MJ. Improved saturation and wide-viewing angle color filters based on multi-twist retarders. Opt Express. 2021;29:4124–38.
41. Yuan R, et al. Spin-decoupled transflective spatial light modulations enabled by a piecewise-twisted anisotropic monolayer. Adv Sci. 2022;9:e2202424.
42. Wei BY, et al. Generating switchable and reconfigurable optical vortices via photopatterning of liquid crystals. Adv Mater. 2014;26:1590–5.
43. Zheng ZG, et al. Three-dimensional control of the helical axis of a chiral nematic liquid crystal by light. Nature. 2016;531:352–6.
44. Liu J, et al. Circularly polarized luminescence in chiral orientationally ordered soft matter systems. Responsive Mater. 2023;1:e20230005.
45. Liu SJ, et al. Bi-chiral nanostructures featuring dynamic optical rotatory dispersion for polychromatic light multiplexing. Adv Mater. 2023;35:e2301714.
46. Shi Y, et al. Two-photon laser-written photoalignment layers for patterning liquid crystalline conjugated polymer orientation. Adv Funct Mater. 2020;31:2007493.

Publisher's Note

Springer Nature remains neutral with regard to jurisdictional claims in published maps and institutional affiliations.